

Weather Estimation for Integrated Sensing and Communication

Victoria Palhares, Artjom Grudnitsky, Silvio Mandelli

Nokia Bell Labs Stuttgart, Germany

Email: {victoria.palhares, artjom.grudnitsky, silvio.mandelli}@nokia-bell-labs.com

Abstract—One of the key features of sixth generation (6G) mobile communications will be integrated sensing and communication (ISAC). While the main goal of ISAC in standardization efforts is to detect objects, the byproducts of radar operations can be used to enable new services in 6G, such as weather sensing. Even though weather radars are the most prominent technology for weather detection and monitoring, they are expensive and usually neglect areas in close vicinity. To this end, we propose reusing the dense deployment of 6G base stations for weather sensing purposes by detecting and estimating weather conditions. We implement both a classifier and a regressor as a convolutional neural network trained across measurements with varying precipitation rates and wind speeds. We implement our approach in an ISAC proof-of-concept, and conduct a multi-week experiment campaign. Experimental results show that we are able to jointly and accurately classify weather conditions with accuracies of 99.38% and 98.99% for precipitation rate and wind speed, respectively. For estimation, we obtain errors of 1.2 mm/h and 1.5 km/h, for precipitation rate and wind speed, respectively. These findings indicate that weather sensing services can be reliably deployed in 6G ISAC networks, broadening their service portfolio and boosting their market value.

Index Terms—6G, ISAC, weather sensing, radar, orthogonal frequency-division multiplexing (OFDM).

I. INTRODUCTION

One of the most prominent and distinctive features of sixth generation (6G) mobile communication systems will be integrated sensing and communication (ISAC). This technology leverages existing communication infrastructure to perform tasks beyond data transmission, such as drone detection, intruder detection, as well as traffic monitoring [1]. Unlike in positioning technologies, where targets actively send and receive signals, sensing targets remain entirely passive. Beyond the aforementioned target detection-focused use cases, ISAC can also be used to monitor weather conditions in the cellular network coverage.

Electromagnetic (EM) waves are affected by atmospheric conditions, e.g., clouds and precipitation, through reflection, absorption, scattering, refraction, and diffraction [2]. These effects are exploited by weather radars, which are the primary deployed technology for weather detection, monitoring, and prediction. These radars emit EM pulses which are partially reflected back to the radar due to the presence of scatterers, and by measuring the propagation time, the distances to the scatterers can be determined. Additionally, the received power provides insights into the size and density of the scatterers. Furthermore, to analyze the motion and speed of weather phenomena, weather radars exploit the Doppler effect. Despite

their accuracy in determining weather conditions over large areas, weather radars are expensive, resulting in their sparse deployment. Moreover, since weather radars are configured to achieve full coverage by mechanically sweeping a limited number of elevation angles over a predefined time, areas in the close vicinity of the radar can be overlooked due to scan timing and revisit constraints [3]. In contrast, ISAC networks are densely deployed and also use EM waves, making them a promising complement or alternative for weather sensing.

A. Contributions

To address weather detection and monitoring at close range, we propose a solution for enabling weather sensing in 6G ISAC networks. In this context, we operate a communication system in a radar-style approach with half-duplex radio units (RUs). By collecting the transmitted and received signals, we estimate the channel state information (CSI). From the estimated CSI, we compute features to be used as input data for our weather estimation supervised learning model. In the presented problem, we perform two different tasks, classification and regression, in order to jointly classify or estimate both precipitation rate and wind speed. We demonstrate the efficacy of our method through experiments with an ISAC proof-of-concept (PoC) [4]. We collect training and test data over multiple weeks in scenarios with and without rain and with variable precipitation rates and wind speeds. For training of the supervised model, we collect reference data from a weather station [5] in close vicinity to the PoC (see Sec. IV-B).

B. Related Work

Recent works on weather radar include [6]–[8]. Both [6] and [7] utilize the interferometric phase diagram as an input for the weather detection algorithm, specifically for classifying rain and no rain conditions. Additionally, [6] incorporates clutter phase alignment and Doppler velocity in its methodology. In contrast, [8] focuses on tracking weather changes over time, analyzing the course and speed of weather phenomena. Unlike these studies, our approach leverages the capabilities of future 6G ISAC networks to estimate weather conditions, not only utilizing existing hardware but also not depending on traditional weather radars.

Most works related to weather monitoring using telecommunication hardware focus on leveraging microwave [9]–[15] or millimeter (mmWave) [16] links. These studies typically utilize links, either point-to-point, backhaul between base stations,

or line-of-sight (LoS) data transmission links, to extract rain measurements. Most of these works concentrate on classifying rain vs. no rain conditions [9], [11] or estimating precipitation rates [9]–[12], [16] by analyzing the signal attenuation on static links instead of the full complex-valued CSI.

Techniques used for rain classification and estimation include single-layer perceptrons [10], support vector machines [9], convolutional neural networks (CNNs) [9], recurrent neural networks [12], long short-term memorys [9], and gated recurrent units [9]. Additionally, some studies focus on creating rainfall maps [13]–[15]. In contrast to these approaches, our method does not rely on microwave static links. Instead, we utilize existing hardware deployed for cellular networks, used for standard communication between next-generation node B-radio units (gNB-RUs) and user equipments (UEs). While we also estimate precipitation rates, our approach differs by leveraging CNNs to process CSI-based periodograms, which are images over range and Doppler shift (speed). These periodograms enables us to perform joint estimation of precipitation rate and wind speed. Furthermore, the aforementioned methods rely on signal attenuation solely from unobstructed fixed links where LoS is assumed, i.e., they are not robust to cluttered environments with multiple obstructions and reflections.

II. DATA PRE-PROCESSING

In this section, we detail the data pre-processing pipeline, from the transmission and reception of orthogonal frequency-division multiplexing (OFDM) frames to the computation of weather features.

A. System Description

We consider a system with a transmitter (Tx) and a receiver (Rx) that operates in half-duplex mode, i.e., can both transmit and receive signals, but not simultaneously. The Tx transmits S frames with M OFDM symbols at carrier frequency f_c over N subcarriers spaced by Δf . We assume analog beamforming, i.e., one active beam at a time. While these transmitted signals propagate to the UEs, they are also reflected by the environment back to the Rx. We define the Tx and Rx OFDM frames as $\mathbf{T}_s, \mathbf{R}_s \in \mathbb{C}^{N \times M}$, for $s \in \mathcal{S} = \{1, \dots, S\}$. In the matrices \mathbf{T}_s and \mathbf{R}_s , the rows and columns represent the subcarriers and OFDM symbols, respectively.

B. CSI Estimation

To estimate weather conditions, we must first provide an estimate of the CSI matrix. The CSI matrix describes the signal propagation between Tx and Rx and captures reflections from multiple scatterers such as buildings, people, drones, and cars. Depending on the ISAC use case, these scatterers might be considered targets or clutter components. Moreover, the CSI matrix also encodes weather phenomena due to multiple effects such as attenuation and reflections caused by weather conditions. These scatterers and weather phenomena affect the Tx OFDM frame by introducing Doppler shifts and propagation delays within the channel between Tx and Rx. For sensing purposes, the Tx OFDM frame \mathbf{T}_s serves only as a reference

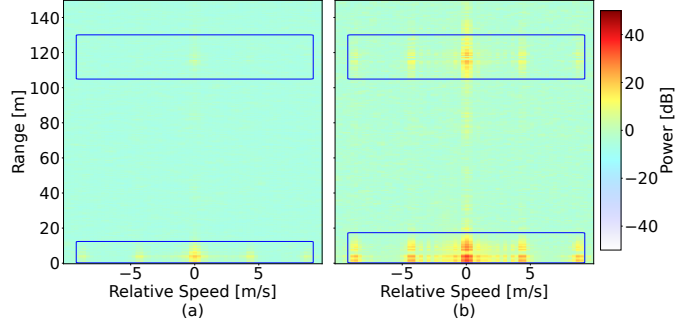


Fig. 1: Comparison between periodograms (a) without rain and (b) with rain. We observe that the rain increases the noise floor of the periodogram and emphasizes the presence of targets around 0 and 120 meters from the Rx.

signal. We estimate the channel by the element-wise division of the Rx OFDM frame \mathbf{R}_s by the Tx OFDM frame \mathbf{T}_s as

$$[\mathbf{H}_s]_{k,l} = \frac{[\mathbf{R}_s]_{k,l}}{[\mathbf{T}_s]_{k,l}}, \quad (1)$$

where $\mathbf{H}_s \in \mathbb{C}^{N \times M}$ is the CSI matrix produced by the s th Tx and Rx frames, k is the row index, and l is the column index. To enable efficient fast Fourier transforms (FFTs) in subsequent weather-feature computation, we zero-pad the CSI matrix $\mathbf{H}_s \in \mathbb{C}^{N \times M}$ to the next power of 2, giving us $\tilde{\mathbf{H}}_s \in \mathbb{C}^{N_{\text{pad}} \times M_{\text{pad}}}$, where $N_{\text{pad}} = 2^{\lceil \log_2 N \rceil}$ and $M_{\text{pad}} = 2^{\lceil \log_2 M \rceil}$.

C. Clutter Removal

We highlight that in the case of weather sensing, radio resources might not be available to acquire measurements from an empty environment without capturing reflections from other scatterers. This environment would be the most suitable for weather detection and estimation, but it is less suitable for communications and other sensing use cases. Thus, to mitigate the effects of clutter, i.e., unwanted scatterers, we apply clutter removal to the zero-padded CSI matrix $\tilde{\mathbf{H}}_s$.

The goal of clutter removal is to suppress environmental components irrelevant to the sensing task. For weather detection and estimation, we are solely interested in analyzing the effects of raindrops, dust particles, and snowflakes, while attenuating the contributions from the surrounding environment (e.g. buildings). For clutter removal, we use the clutter removal with acquisitions under phase noise (CRAP) algorithm [17]. We refer to the CSI matrix after CRAP as $\hat{\mathbf{H}}_s \in \mathbb{C}^{N_{\text{pad}} \times M_{\text{pad}}}$. This algorithm requires a calibration matrix, which we compute based on measurements of the previous day with the lowest precipitation rate and wind speed.

D. OFDM Radar Processing

The next step towards weather detection and estimation is periodogram generation. A periodogram estimates a signal's power spectral density, highlighting its dominant spectral components, and is computed via a series of FFTs. In the case of this work, we aim to compute a two-dimensional (2D) periodogram that enables us to detect targets at various ranges

(delays) and Doppler shifts (relative speeds) [18]. Considering our analog beamforming assumption and no beam sweeping, in this work, we disregard antenna and angular information. More specifically, we focus on analyzing the effect of weather elements such as raindrops, dust particles, and snowflakes in the periodogram. Since the input of the periodogram computation is a 2D CSI matrix, we extend the periodogram calculation as follows:

$$\begin{aligned} [\hat{\mathbf{P}}_s]_{n,m} &= \frac{1}{NM} \sum_{k=0}^{N_{\text{pad}}-1} \left[\sum_{l=0}^{M_{\text{pad}}-1} [\hat{\mathbf{H}}_s]_{k,l} e^{-j2\pi \frac{lm}{M_{\text{pad}}}} \right] e^{j2\pi \frac{kn}{N_{\text{pad}}}} \\ &= \frac{1}{NM} \mathcal{F}^{-1} \left\{ \mathcal{F} \left\{ [\hat{\mathbf{H}}_s]_{k,l} \right\} \right\}, \end{aligned} \quad (2)$$

In (2), we perform N FFTs of length M_{pad} that take the CSI matrix from time (OFDM symbols) to Doppler shift (relative speed) domain and M inverse FFTs (IFFTs) of length N_{pad} that take the CSI matrix from frequency (subcarriers) to delay (range) domain. We crop the periodogram $\hat{\mathbf{P}}_s \in \mathbb{C}^{N_{\text{pad}} \times M_{\text{pad}}}$ to $[1, \dots, N']$ rows and $[\lfloor [M_{\text{pad}} - M']/2 \rfloor + 1, \dots, \lfloor [M_{\text{pad}} - M']/2 \rfloor + M']$ columns according to the desired evaluation range, i.e., the interval of ranges and relative speeds that we are interested in. We highlight that in the case of relative speed, the cropping is centered around zero. The calculation of N' range bins and M' speed bins can be carried out according to [18]. In this way, from a 2D CSI matrix $\mathbf{H}_s \in \mathbb{C}^{N \times M}$ over subcarriers and OFDM symbols, we obtain a 2D complex periodogram $\mathbf{P}_s \in \mathbb{C}^{N' \times M'}$ over range (delay) and Doppler shift (relative speed).

E. Feature Engineering

In Fig. 1, we present the absolute-value squared periodograms $|\mathbf{P}_s|^2$ for a scenario without and with rain, where the rain-induced effects are clearly visible, as highlighted by the blue rectangles in the figure. Accordingly, in this work we propose using the 2D periodograms as input data to compute the features of the weather detection and estimation problem.

In this work, we consider that the Tx emits waves in polarization ρ_1 and that the Rx receives waves both in polarization ρ_1 and ρ_2 . Therefore, we can generate complex periodograms for two polarization combinations: $\rho_1-\rho_1$ ($\mathbf{P}_s^{\rho_1\rho_1}$) and $\rho_1-\rho_2$ ($\mathbf{P}_s^{\rho_1\rho_2}$). In the first case, the CSI matrix is computed using Tx and Rx OFDM frames from polarization ρ_1 . In the second case, the CSI matrix is computed using Tx OFDM frames from polarization ρ_1 and Rx OFDM frames from polarization ρ_2 . In addition, we decompose the complex periodogram into its real and imaginary parts. Thus, we have the following three-dimensional (3D) feature tensor $\mathbf{F}_s \in \mathbb{R}^{N' \times M' \times L}$ with $L = 4$ channels:

$$[\mathbf{F}_s]_{n,m,1} = \Re \left\{ [\mathbf{P}_s^{\rho_1\rho_1}]_{n,m} \right\} \quad (3)$$

$$[\mathbf{F}_s]_{n,m,2} = \Im \left\{ [\mathbf{P}_s^{\rho_1\rho_1}]_{n,m} \right\} \quad (4)$$

$$[\mathbf{F}_s]_{n,m,3} = \Re \left\{ [\mathbf{P}_s^{\rho_1\rho_2}]_{n,m} \right\} \quad (5)$$

$$[\mathbf{F}_s]_{n,m,4} = \Im \left\{ [\mathbf{P}_s^{\rho_1\rho_2}]_{n,m} \right\}, \quad (6)$$

where n and m are the indices of the first and second dimension of the tensor, respectively. After computing the 3D feature tensor \mathbf{F}_s from each CSI matrix \mathbf{H}_s , we normalize the matrices so as to improve convergence on the weather detection and estimation problem. Specifically, we perform a channel-wise normalization: for each channel $\ell = 1, \dots, L$, the data is normalized across all samples S , N' rows, and M' columns, such that each channel has zero mean and unit standard deviation. We define the normalized 3D feature tensor as $\bar{\mathbf{F}}_s$. The set of tensors $\{\bar{\mathbf{F}}_s\}_{s \in \mathcal{S}}$ forms the feature dataset.

III. WEATHER ESTIMATION

We now present the weather detection and estimation problem through two different tasks: classification and regression. The goal of these tasks is to jointly detect and estimate $W = 2$ weather metrics $w \in \{1, 2\}$: precipitation rate ($w = 1$) and wind speed ($w = 2$). For these tasks, we can learn a function $g_\theta : \mathbb{R}^{N' \times M' \times L} \rightarrow \mathbb{R}^{C_w}$ that maps feature tensors to estimates of weather metrics $\hat{\mathbf{x}}_{s,w} \in \mathbb{R}^{C_w}$, for $w \in \{1, 2\}$, as

$$\hat{\mathbf{x}}_{s,w} = g_\theta(\bar{\mathbf{F}}_s) \in \mathbb{R}^{C_w} \text{ for } w \in \{1, 2\}, \quad (7)$$

where C_w is the number of classes of the specific weather metric w . We implement g_θ as a CNN with weights and biases described by θ .

A. Task I: Classification

A classification problem entails learning a mapping from features to a finite set of discrete classes. We learn the classification function g_θ with a cross-entropy loss as

$$\mathcal{L}_{\text{class}} = \sum_{w=1}^W \sum_{s=1}^S -\phi_{w,y} \log \left[\frac{\exp([\hat{\mathbf{x}}_{s,w}]_y)}{\sum_{j=1}^{C_w} \exp([\hat{\mathbf{x}}_{s,w}]_j)} \right], \quad (8)$$

where $\phi_{w,y}$ is the weight of the class y in task w , $[\hat{\mathbf{x}}_{s,w}]_y$ is the output of the CNN for sample s in weather metric w and class y , and class $y = y_{s,w}$ is the correct label for frame s and weather metric w . The predicted label for frame s and weather metric w is then

$$\hat{y}_{s,w} = \max_{j=1, \dots, C_w} (\hat{\mathbf{x}}_{s,w})_j. \quad (9)$$

B. Task II: Regression

A regression problem entails estimating a continuous value based on the input data. Since we have no classes in this case, we assume that $C_w = 1$, for $w = 1, 2$. We learn the regression function g_θ with a mean squared error (MSE) as

$$\mathcal{L}_{\text{reg}} = \sum_{w=1}^W \frac{1}{S} \sum_{s=1}^S |\hat{x}_{s,w} - y_{s,w}|^2, \quad (10)$$

where $\hat{x}_{s,w}$ is the output of the CNN and $y_{s,w}$ is the reference data, both for sample s and weather metric w . The predicted label for sample s and weather metric w is then

$$\hat{y}_{s,w} = \hat{x}_{s,w}. \quad (11)$$

Both loss functions in (8) and (10) rely on reference data for all training samples, i.e. it is a supervised learning problem.

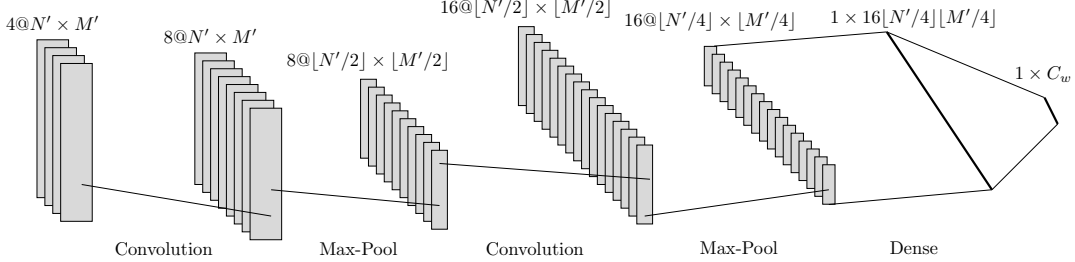


Fig. 2: CNN architecture for weather detection and estimation problem.

C. CNN Architecture

As illustrated in Fig. 2, g_θ is implemented as a CNN with the following structure:

- Convolutional layer with 4 input channels, 8 output channels, kernel size of 3×3 , stride of 1, and padding of 1.
- Max pooling layer with kernel size of 2×2 , stride of 2 and padding of 0.
- Convolutional layer with 8 input channels, 16 output channels, kernel size of 3×3 , stride of 1, and padding of 1.
- Max pooling layer with kernel size of 2×2 , stride of 2 and padding of 0.
- Flatten layer that vectorizes the 2D output of the max pooling layer into a one-dimensional vector.
- Fully connected layer with input size of $16 \lfloor N'/4 \rfloor \lfloor M'/4 \rfloor$ and output size C_w , i.e., according to the weather metric w .

These hyperparameters were chosen heuristically after multiple experiments with a pre-trained ResNet-18 [19] and custom CNNs built from scratch with varying numbers of convolutional and pooling layers, channel sizes (e.g., 32, 64, 96, 128), and kernel sizes (e.g., 5, 6). The final selection was based on computational complexity and the resulting training and validation losses.

IV. EXPERIMENTAL RESULTS

In this section, we provide details about the used ISAC PoC, as well as describe the collection of weather data used in the supervised learning problems. Furthermore, we describe the performance metrics used and showcase the effectiveness of the proposed method through experimental results.

A. PoC Setup

Figs. 4a, 4b show the deployment of the ISAC PoC which consists of:

- 2 RUs, a gNB-RU acting as a Tx and a sniffer acting as Rx (see Fig. 4a). Each RU consists of 2 single-polarized (vertical and horizontal, ρ_1 and ρ_2 , as defined in Sec. II-E) uniform rectangular arrays, consisting of 8×12 antenna elements each. Transmission on a single polarization allows up to 52 dBm effective isotropic radiated power (EIRP). The RUs support analog beamforming, with the ISAC PoC allowing for beam switching at each radio frame.

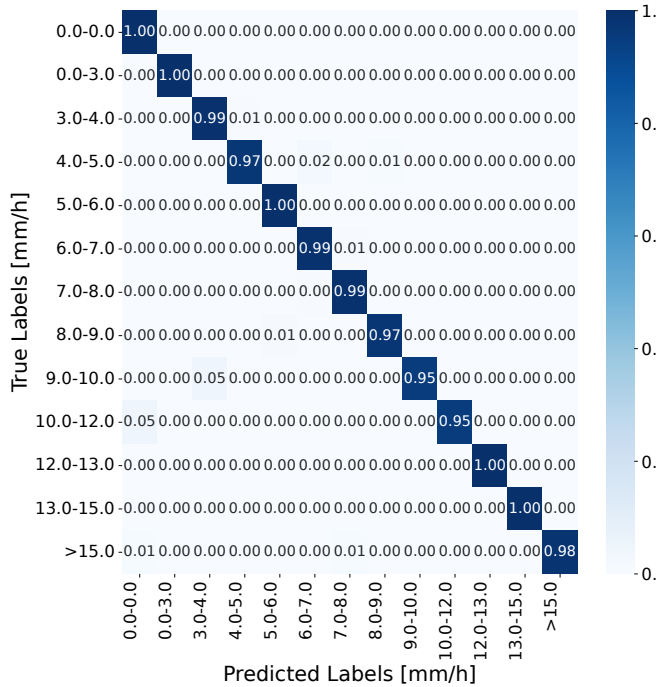
- a server responsible for sensing processing, the sensing processing unit (SPU) (see Fig. 4b), including periodogram computation and weather detection and estimation.
- a synchronization source (see Fig. 4b) for the antennas and server.

The Tx and Rx antennas are collocated in a quasi mono-static configuration. The deployment location of the antennas is the roof of a 5 story office building within a city. The antennas are fifth generation (5G) mmWave RUs for Tx and Rx, conforming to the evolved common public radio interface (eCPRI) split 7.2x [20]. The PoC uses 5G $\mu = 3$ numerology. Each radio frame consists of $M = 1120$ OFDM symbols over $N = 1584$ subcarriers spaced by $\Delta f = 120$ KHz within a bandwidth of 200 MHz. We use a center frequency of $f_c = 27.6$ GHz, as available in our over-the-air license for our outdoor deployment. For the PoC, we use a pre-recorded OFDM test frame, which is continuously transmitted over the fronthaul link from the SPU to the gNB-RU. Each subcarrier in the test frame is modulated with a random QPSK constellation point. This test frame is emitted by the gNB-RU towards the environment and the signal reflected by the environment is then received by the sniffer, transmitted over fronthaul to the SPU, which then performs CSI and periodogram computation, as described in Sec. II. Further details on the PoC are available in [4].

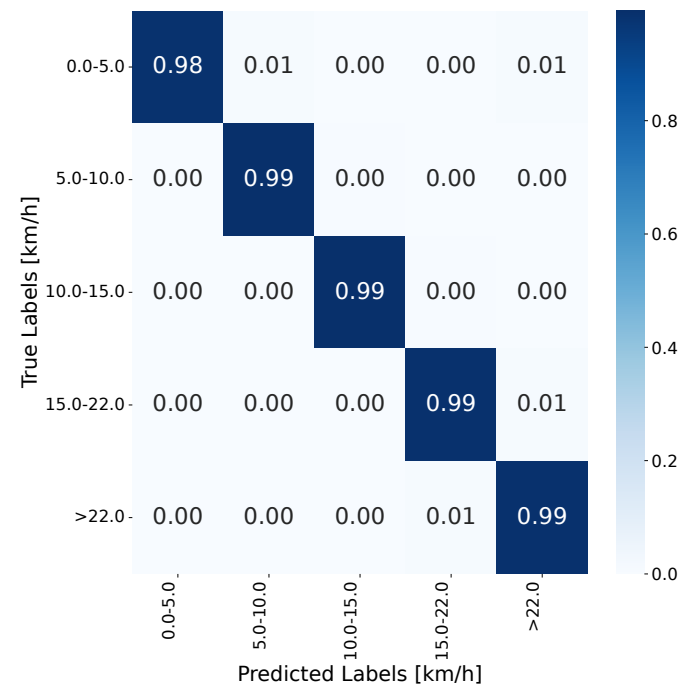
B. Weather Data Collection

We gather the training data, i.e., the Tx and Rx OFDM frames in the following fashion: We trigger a rain/no rain check every 2 minutes. If it is raining, we record a measurement. If it is not raining, we record non-rain measurements every 10 minutes. A measurement is recorded for 1 second, gathering a total of 100 OFDM frames, both for Tx and Rx. The choice for this criteria is storage issues and the predominance of non-rain scenarios.

We gather the reference values for the supervised learning tasks (see Sec. III-A and Sec. III-B) with the use of a weather station (see Fig. 4c) [5]. The device is installed in close vicinity to the ISAC PoC and periodically records measurements for precipitation rate (mm/h), wind speed (km/h), among other metrics. We pair the training data with the reference values based on closeness in time. For the classification problem (see Sec. III-A), we map the acquired data to classes presented in the axes of Fig. 3a and Fig. 3b.



(a) Precipitation rate classification accuracy



(b) Wind speed classification accuracy

Fig. 3: Normalized confusion matrices of the (a) precipitation rate and (b) wind speed classification accuracy.

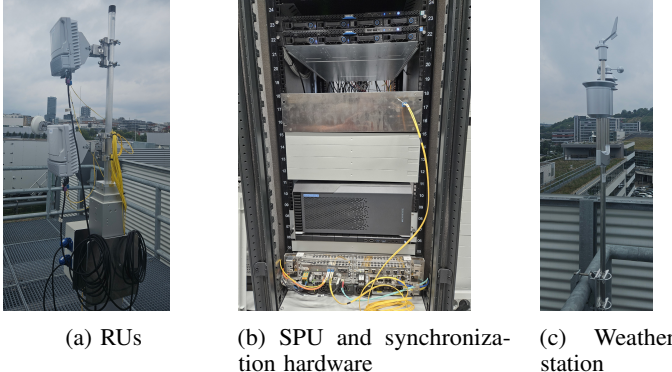


Fig. 4: ISAC PoC deployment for weather sensing experiments.

C. Training Parameters

The dimensions of the CSI matrix after zero-padding, $\bar{\mathbf{H}}$, are $N_{\text{pad}} = M_{\text{pad}} = 2048$. For periodogram evaluation, we crop the periodogram to a range of $[0, 450]$ meters and a Doppler shift of $[-10, +10]$ m/s, corresponding to $N' = 746$ range bins and $M' = 68$ speed bins. For training and testing, we use $S_{\text{train}} = 9786$ and $S_{\text{rain}} = 9780$ samples of no-rain and rain scenarios, respectively, giving a total of $S = 19566$ samples. On each of these sets, we separate 80% and 20% of the dataset for training and testing, respectively. For training and testing, we use 158 and 39 batches, respectively, with a batch size of 100 samples. To ensure a balanced representation across scenarios, each batch is constructed with 50 frames from the no-rain dataset and 50 frames from the rain dataset. For training, we use the Adam optimizer. The proposed model was implemented

in PyTorch (v2.5.1) with CUDA support (v12.1) and trained on an NVIDIA GPU. All results and performance metrics are computed using the test set.

D. Performance Metrics

Here we describe the performance metrics used for classification and regression, respectively.

1) *Classification*: For classification, we present our results as normalized confusion matrices, which indicate how many samples out of all samples were correctly classified in each class for each weather metric.

2) *Regression*: For regression, we present our results as cumulative distribution functions (CDFs) of the estimation error $|\hat{y}_{s,w} - y_{s,w}|$ for each weather metric and summarize the curves by looking at the mean and 90-percentile, which we define as $\text{Pr}[X \leq x] = 0.9$.

E. Performance Results

1) *Classification*: For the following experiments, we consider that 50% of the samples have a precipitation rate equal to 0 mm/h, while the other 50% are distributed among varying precipitation rates.

In Figs. 3a and 3b, we present the normalized confusion matrices for both precipitation rate and wind speed based on test set classification. For precipitation rate and wind speed, the classification accuracy is 99.38% and 98.99%, respectively.

2) *Regression*: In Figs. 5a and 5c, we present both the precipitation rate and wind speed data distribution on the test set. As we can observe, precipitation rate lies within the interval

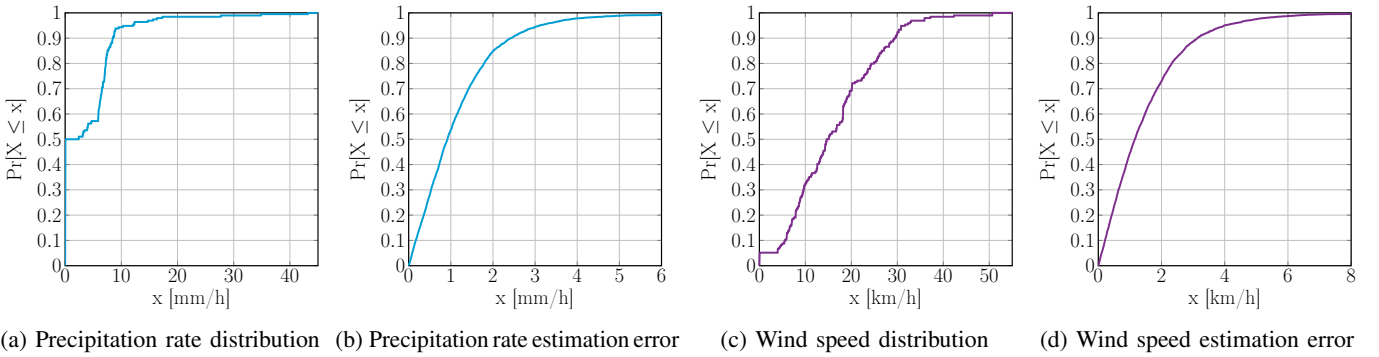


Fig. 5: CDFs of the (a) precipitation rate distribution, (b) precipitation rate estimation error, (c) wind speed distribution, and (d) wind speed estimation error.

of $[0, 43.2]$ mm/h while wind speed lies within the interval of $[0, 50.7]$ km/h.

In Figs. 5b and 5d, we present the CDFs for both the precipitation rate and wind speed estimation errors based on inference on the test set. In our experiments, the precipitation rate achieves a mean error (ME) of 1.2 mm/h and a 90-percentile error of 2.43 mm/h while the wind speed achieves an ME of 1.5 km/h and a 90-percentile error of 3.14 km/h.

V. CONCLUSIONS AND FUTURE WORK

We have proposed a solution to enable weather sensing in 6G ISAC networks, and have validated our approach with extensive measurements on a realistic setup. We have performed weather estimation using CSI-based periodograms as inputs to two supervised learning tasks, classification and regression, implemented as a CNN. The proposed method has enabled us to jointly detect and estimate weather phenomena such as precipitation and wind, solely using communication signals.

Our experiments with measurements from the ISAC PoC have demonstrated that we are capable of achieving accuracies of 99.38% and 98.99% for the classification of precipitation rate and wind speed, respectively. We have also shown that by using our method, we can achieve an average estimation error of 1.2 mm/h and 1.5 km/h for precipitation rate and wind speed, respectively. These results show good promises for the deployment of weather sensing in future 6G ISAC networks.

There are several avenues for future work. First, improving the generalization of our method through transfer learning. Second, performing experiments in other frequency bands, e.g., FR1 ($f_c = 3.5$ GHz). Third, considering a fully mono-static configuration, where the RU operates in full-duplex mode.

REFERENCES

- [1] S. Mandelli, M. Henninger, M. Bauhofer, and T. Wild, “Survey on integrated sensing and communication performance modeling and use cases feasibility,” in *Int. Conf. 6G Netw. (6GNet)*, Oct. 2023, pp. 1–8.
- [2] T. Oguchi, “Electromagnetic wave propagation and scattering in rain and other hydrometeors,” *Proc. IEEE*, vol. 71, no. 9, pp. 1029–1078, Sep. 1983.
- [3] R. D. Palmer, M. B. Yeary, D. Schwartzman, J. L. Salazar-Cerreno *et al.*, “Horus—a fully digital polarimetric phased array radar for next-generation weather observations,” *IEEE Trans. Radar Syst.*, vol. 1, pp. 96–117, May 2023.
- [4] T. Wild, A. Grudnitsky, S. Mandelli, M. Henninger *et al.*, “6G integrated sensing and communication: From vision to realization,” in *Eur. Radar Conf. (EuRAD)*, Sep. 2023, pp. 355–358.
- [5] Homematic. (2024) Homematic IP Weather Sensor-Plus. [Online]. Available: <https://homematic-ip.com/de/produkt/wettersensor-plus>
- [6] Q. Yu, D. Wu, D. Zhu, and J. Qian, “CNN-based weather signal detection algorithm for airborne weather radar,” in *Int. Conf. Signal Image Process. (ICSIP)*, Oct. 2020, pp. 660–664.
- [7] Y. Wang, D. Wu, D. Zhu, and F. Meng, “Detection of weather signal in ground clutter for airborne weather radar based on spatial processing in elevation,” in *IEEE Int. Conf. Signal Image Process. (ICSIP)*, Oct. 2020, pp. 655–659.
- [8] G. Villa, J. A. Ruiz, C. Da Costa, J. L. Corrales *et al.*, “Enhanced weather detection and tracking algorithms in primary surveillance radar,” in *Integr. Commun. Navig. Surveill. Conf. (ICNS)*, Apr. 2024, pp. 1–7.
- [9] B. Lian, Z. Wei, X. Sun, Z. Li *et al.*, “A review on rainfall measurement based on commercial microwave links in wireless cellular networks,” *Sensors*, vol. 22, no. 12, Jun. 2022.
- [10] A. Daher, H. Al Sakka, and A. K. Chaaban, “Low complexity single-layer neural network for enhanced rainfall estimation using microwave links,” *J. Hydroinf.*, vol. 25, no. 1, pp. 101–112, Dec. 2022.
- [11] P. Zhang, X. Liu, and K. Pu, “Precipitation monitoring using commercial microwave links: Current status, challenges and prospectives,” *Remote Sensing*, vol. 15, no. 19, Oct. 2023.
- [12] D. Jacoby, J. Ostrometzký, and H. Messer, “Integrated RNNs for rainfall sensing with wireless communication networks,” in *IEEE Int. Conf. Acoust. Speech Signal Process. Workshops (ICASSPW)*, Apr. 2024, pp. 419–423.
- [13] N. Blettner, M. Fencl, V. Bareš, H. Kunstmänn *et al.*, “Transboundary rainfall estimation using commercial microwave links,” *Earth Space Sci.*, vol. 10, no. 8, Aug. 2023.
- [14] A. Overeem, H. Leijnse, T. C. van Leth, L. Bogerd *et al.*, “Tropical rainfall monitoring with commercial microwave links in Sri Lanka,” *Environ. Res. Lett.*, vol. 16, no. 7, p. 074058, Jul. 2021.
- [15] M. Djibo, C. Chwala, M. Graf, J. Polz *et al.*, “High-resolution rainfall maps from commercial microwave links for a data-scarce region in west Africa,” *J. Hydrometeorol.*, vol. 24, no. 10, pp. 1847 – 1861, Oct. 2023.
- [16] C. Han, Y. Bi, S. Duan, and G. Lu, “Rain rate retrieval test from 25-GHz, 28-GHz, and 38-GHz millimeter-wave link measurement in Beijing,” *IEEE J. Sel. Topics Appl. Earth Observ. Remote Sens.*, vol. 12, no. 8, pp. 2835–2847, Jul. 2019.
- [17] M. Henninger, S. Mandelli, A. Grudnitsky, T. Wild *et al.*, “CRAP: Clutter removal with acquisitions under phase noise,” in *Int. Conf. 6G Netw. (6GNet)*, Oct. 2023, pp. 1–8.
- [18] M. Braun, “OFDM radar algorithms in mobile communication networks,” Ph.D. dissertation, Karlsruhe Institute of Technology, 2014.
- [19] K. He, X. Zhang, S. Ren, and J. Sun, “Deep residual learning for image recognition,” in *IEEE Conf. Comput. Vis. Pattern Recognit. (CVPR)*, Jun. 2016, pp. 770–778.
- [20] *O-RAN Control, User and Synchronization Plane Specification 19.0*, O-RAN ALLIANCE e.V., 2025, <https://specifications.o-ran.org/download?id=952>.